Research Paper

Synergistic Ag/TiO$_2$-N photocatalytic system and its enhanced antibacterial activity towards *Acinetobacter baumannii*

Guoxiang Yang[a,1], Haibo Yin[a,1], Wenhua Liu[a], Yuping Yang[a], Quan Zou[a], Liulin Luo[b,*], Huiping Li[c], Yuning Huo[a,*], Hexing Li[a,*]

[a] *The Education Ministry Key Lab of Resource Chemistry, Shanghai Key Laboratory of Rare Earth Functional Materials, Shanghai Normal University, Shanghai 200234, China*
[b] *Department of Clinical Laboratory Medicine, Shanghai Pulmonary Hospital, Tongji University School of Medicine, Shanghai 200433, China*
[c] *Department of Respiratory Medicine, Shanghai Pulmonary Hospital, Tongji University School of Medicine, Shanghai 200433, China*

ABSTRACT

The hybrid Ag/TiO$_2$-N photocatalyst was prepared *via a* supercritical solvothermal process in ethanol fluid. The simultaneous achievement of reduction of Ag$^+$ ions and N-doping in silver-ammonia complex solution led to the uniform distribution of Ag nanoparticles stably combined with the surface of TiO$_2$-N substrate. As a result, the visible-light photocatalytic inactivation of *Acinetobacter baumannii* was facilitated *via* the enhanced visible light harvesting and the high separation efficiency of photo-induced charge carriers. By means of the main active species of ·O$_2$$^-$ radical, the synergistic effect of Ag nanoparticles and TiO$_2$-N could induce the structure change of bacteria with the leakage of K$^+$ ions as well as the mineralization of cell membrane with the elimination of self-repair function, leading to the final cell death. In comparison, the bactericidal activity of Ag nanoparticles and TiO$_2$-N under UV light irradiation was due to the intrinsic efficiency and the high light harvesting, respectively. The photothermal effect of Ag nanoparticles in the near-IR light region could be possibly remained by TiO$_2$-N substrate to achieve the antibacterial activity. Furthermore, Ag/TiO$_2$-N photocatalyst played great bactericidal effect for kinds of bacteria, implying the applicable future to the medical disinfection.

1. Introduction

Disinfectants to various bacteria are crucial for reducing pathogenic microorganisms since microbial contamination has always been the challenge that threats the health of human beings and the safety of water and food production [1,2]. Up to now, many antibacterial methods, such as antibiotics and UV light, are popularly used all over the world due to the broad-spectrum antibacterial capacities. However, its harm on human health safety and the antibiotic resistance encourages people to find new alternative antibacterial candidates [3,4]. Therefore, it is very necessary to develop antibacterial treatment methods which are effective, low-cost, and environmental friendly [5]. As we known, the traditional antibacterial applications, including chlorination and ozonation disinfection, are often chemically, energetically, and operationally intensive [6]. In comparison, photocatalysis has been considered as a powerful route owing to the ability of fatal damage to a wide range of pathogenic microorganisms including those are resistant to other disinfection methods, in addition to the utilization of solar light, and the environmental friendship with less or even no disinfection by-product formation [7,8]. Photoactive TiO$_2$ has been proved to be effective for the disinfection capability and the most suitable for wide-spread environment application for its high chemical stability, non-toxicity and low cost [9]. The reactive oxygen species (ROS) generated by TiO$_2$ under UV light irradiations can cause oxidative damage to cell membranes and inactivate microorganisms [10]. Meanwhile, many metallic nanomaterials such as Ag nanoparticles have attracted great attention due to their intrinsic antimicrobial activity. Their possible antibacterial mechanisms include the release of toxic metal ions, generation of reactive oxygen species, and the direct contact to the cell membrane [11–13]. However, the popular utilization of either photocatalytic metallic oxides or metallic nanoparticles as a disinfectant still has obvious limitations. For example, TiO$_2$ photocatalyst has little bacteriostatic activity under the visible-light irradiations. The release of Ag ions during the difficult separation from the water may cause the adverse environmental risk and human health effects [14]. Expectedly, the combination of Ag nanoparticles with TiO$_2$ has

---

* Corresponding authors.
  E-mail addresses: luoliulin@sina.com (L. Luo), huoyuning@shnu.edu.cn (Y. Huo), hexing-li@shnu.edu.cn (H. Li).
[1] Guoxiang Yang and Haibo Yin contributed equally to this work.

attracted wide attentions in recent years, since Ag nanoparticles can extend the light absorption spectrum of TiO_2 toward the visible-light region due to the surface plasma effect and promote the separation of photo-generated electron-hole pairs by creating the Schottky barrier to facilitate the electron transfer from TiO_2 to Ag nanoparticles [15]. However, the powerful Ag-TiO_2 hybrid is still in need of further exploration for the stable combination, and the intrinsic antimicrobial mechanism for the synergistic effect of Ag and TiO_2 in the photocatalytic composite is still not well understood [16]. Therefore, it is essential to develop the novel routes to achieve the stable hybrid of TiO_2 with Ag nanoparticles for the antibacterial process by carrying forward the advantages of both materials.

Up to now, various methods such as aqueous reduction, photochemical and aerosol process have been applied to prepare the Ag/TiO_2 composites. For example, the aqueous preparation of Ag/TiO_2 film was reported by Kuo [17] and the active black TiO_2-Ag/TiO_x particles *via* the flame aerosol technology was reported by Pratsinis [18]. However, the leakage of Ag nanoparticles from TiO_2 still limits their synergistic effect to achieve the efficient inactivation of bacteria. The supercritical solvothermal process has been considered as an efficient route for the preparation of nanocomposites. It provides the powerful way for the controllable nanostructures within short reaction time and without any further high-temperature heat treatments [19], and maintains the nanoscale architecture during the removal of the solvent [20]. More importantly, the supercritical fluid encourages the combination of nanoparticles by the high pressure and temperature, and leads to the uniform nanoparticles with the high crystal nucleation rates and little subsequent crystal growth [21–23]. It mainly results from the gas-like diffusivity and zero surface tension of supercritical fluid as well as the low viscosity of the reactants in the supercritical fluid [24–26].

Herein, we reported the hybrid Ag/TiO_2-N nanoparticles with the stable combination *via* a supercritical solvothermal process in ethanol fluid, in which the Ag^+ ions could be directly reduced without additional reductant to avoid the formation of byproduct. The precursor of silver-ammonia complex solution could induce the uniform and stable deposition of Ag nanoparticles on the TiO_2 surface and the simultaneously doping of N element to facilitate the photocatalytic antibacterial capability. As we known, *Acinetobacter baumannii* (A. *baumannii*) belongs to the genus Acinetobacter which is a genetically diverse group of aerobic, gram-negative and non-fermenting bacteria. A. *baumannii* is emerging as an opportunistic pathogen due to the increased multidrug resistance and results in therapy failure [27,28]. It has induced extensive nosocomial infections and has attracted particular attention in intensive care unit (ICU) patients [29]. These infections are extremely difficult to treat due to its multiple or pandrugs resistance [30], and even resistant to the low concentration of disinfecting agents [31]. The present Ag/TiO_2-N nanoparticles revealed the powerful photocatalytic activity for the elimination of A. *baumannii* as well as other bacteria. The synergistic effect of Ag nanoparticles and TiO_2-N could lead to the complete destruction and mineralization of A. *baumannii* with the elimination of self-repair function.

2. Experimental

2.1. Reagents

All reagents and materials involved were of analytical purity. They were obtained commercially from the Aladdin and used as received without further purification. Ultra-pure water was used during the experimental process. The experiments were carried out at room temperature and humidity.

2.2. Preparation of Ag/TiO_2-N catalyst

Ag/TiO_2-N samples were synthesized *via* a supercritical solvothermal route. At first, 10 mL tetrabutyl titanate was dissolved in

30 mL absolute ethanol. After stirring at 25 °C for 30 min, the precursor solution was transferred into a 500 mL autoclave containing 170 mL absolute ethanol. Then, it was heated to the ethanol supercritical point (243 °C and 6.4 MPa) at the speed of 2 °C/min, which was determined as the optimal conditions for the photocatalytic antibacterial process. After being treated under this supercritical condition for 70 min, the system was allowed to cool slowly to room temperature naturally. The precipitate was centrifuged, washed with distilled water and ethanol for 3 times, and dried at 80 °C for 24 h to obtain the pure TiO_2 samples. Then, 0.5280 g TiO_2 powder was ultrasonically dispersed in 50 mL ethanol for 1 h to form the suspension. The desired amount of $AgNO_3$ was dissolved into 10 mL ultra-pure water followed by adding 0.8 mL aqueous ammonia to form the silver-ammonia complex solution. After adding the complex solution into TiO_2 suspension, it was transferred into a 500 mL autoclave containing 170 mL absolute ethanol and was heated to the supercritical condition again (243 °C and 6.4 MPa). After being treated for 70 min, the system was allowed to cool slowly to room temperature naturally. The precipitate was centrifuged, washed with distilled water and ethanol for 3 times, and dried at 80 °C for 24 h to obtain the Ag/TiO_2-N samples. The as-prepared samples denoted as X% Ag/TiO_2-N, in which X value represented the actual Ag/Ti molar ratio. The N/Ti molar ratios were determined as about 0.073 mol% in various N-doped samples, based on the N and Ti characteristic peaks of X-ray photoelectron spectroscopy (XPS) by using 0.477 and 2.001 as the PHI sensitivity factors.

For comparison, other reference samples were prepared as follows. (1) TiO_2-N sample was prepared without $AgNO_3$ as the above process. The actual amount of N species was adjusted as that in X%Ag/TiO_2-N. (2) 4.0%Ag/TiO_2 sample was obtained without aqueous ammonia during the above reaction process. (3) 4.0%Ag/TiO_2-N(I) was obtained by the *in-situ* supercritical solvothermal process. 10 mL tetrabutyl titanate was dissolved in 30 mL absolute ethanol. After stirring at 25 °C for 30 min, the desired amount of silver-ammonia complex solution was added. Then, the precursor solution was heated to the ethanol supercritical point (243 °C and 6.4 MPa) for 70 min. The following process was same as that of X%Ag/TiO_2-N. (4) 4.0%Ag/TiO_2-N(P) was prepared by photo-reduction route. 0.5280 g TiO_2 powder obtained in the above supercritical solvothermal process was added in 150 mL absolute ethanol with silver-ammonia complex solution. Then, the solution was irradiated for 15 min under 3 W LED light with the wavelength of 365 nm. The obtained powder was washed with ethanol and deionized water for at least 3 times and dried at ambient temperature for 1 h. (5) 4.0%Ag/TiO_2-N(S) was prepared by the solvothermal route. The desired amount of silver-ammonia complex solution was added into 150 mL absolute ethanol containing 0.5280 g TiO_2 powder which was obtained *via* the above supercritical solvothermal process. Then, the precursor solution was transferred into a 50 mL Teflon-lined stainless-steel autoclave and maintained at 190 °C for 70 min followed by naturally cooling to room temperature. The obtained powder was washed with ethanol and deionized water for at least 3 times and dried at ambient temperature for 1 h. (6) 4.0%Pd/TiO_2-N was prepared by the supercritical solvothermal method. 0.356 g $HPtCl_6$ was dissolved in 50 mL absolute ethanol containing 0.8 mL $NH_3 \cdot H_2O$ and 0.5280 g TiO_2 powder obtained *via* the above supercritical solvothermal process. Then, the mixture was heated to the ethanol supercritical point (243 °C and 6.4 MPa) for 70 min. The following process was same as that of X%Ag/TiO_2-N. The amount of N species in 4.0%Pd/TiO_2-N was same as that in 4.0%Ag/TiO_2-N. (7) 4.0%Ag/SiO_2 was synthesized by the supercritical solvothermal process. The desired amount of silver-ammonia complex solution was added into 50 mL absolute ethanol containing 0.5280 g commercial SiO_2 powder. Then, the precursor solution was heated to the ethanol supercritical point (243 °C and 6.4 MPa) for 70 min. The following process was same as that of X%Ag/TiO_2-N. (8) Ag nanoparticles were prepared *via* the removal of SiO_2 in 4.0%Ag/SiO_2 by being dissolved in 2 mol/L NaOH solution (NaOH/SiO_2 molar ratio = 10:1.0) at 40 °C for 12 h.

2.3. Characterization

The structure of catalysts was determined by X-ray diffraction (XRD) patterns on Rigacu Dmax-3C (Cu Kα radiation). The morphologies of the materials were observed and analyzed by transmission electronic micrograph (TEM) on a JEM-2010 and field-emission scanning electron microscopy (FESEM, Hitachi S-4800). The N_2 adsorption-desorption isotherms were obtained on a NOVA 4000 at 77 K, from which the specific surface area (S_{BET}), pore volume (V_P), and average pore diameter (D_P) were calculated by using BJH method. The thermogravimetric and differential thermal analysis (TG-DTA) curves were recorded on a TGA, DTG-60H instrument at a heating rate of 10 °C/min using α-Al_2O_3 as the standard material in air. UV–vis diffuse reflectance spectra (UV-vis DRS) and photoluminescence spectra (PLS) were conducted on MC-2530 and Varian Cary-Eclipse 500, respectively. The same amount of sample was confirmed for the comparison in each measurement. The X-ray photoelectron spectroscopy (XPS) analysis was performed on a Perkin-Elmer PHI 5000C. All the binding energies were calibrated by using the contaminant carbon (C_{1S}, 284.6 eV) as a reference. The metal ion concentrations were determined by using inductively coupled plasmatomic emission spectroscopy (ICP, VISTA-MPX). The Photothermal imaging was recorded on an FLIR A300 camera with a near-IR laser (λ = 808 nm, absolute powers of 5.2 W) from Shanghai Xilong Optoelectronics Technology Co., Ltd.

2.4. Bacteria culture

The A. *baumannii* was grown in blood agar at 37 °C for 18 ∼ 24 h. Single clones were selected and the suspension was adjusted to 0.5 MFC, corresponding to the yield of a bacteria count of approximate 10^8 CFU/mL. Then, the bacterial cells were collected by centrifugation (5000g for 10 min), re-suspended and gradient diluted in phosphate-buffered saline (PBS).

2.5. Photocatalytic inactivation test of bacteria

Firstly, 60 mg catalysts were uniformly dispersed in 20 mL 9% NaCl solution by ultrasonication for 2 min 300 uL suspension system was added into 15 mL bacteria solution (0.5 MCF). Then, the obtained mixture was stirred at 800 rpm irradiated under one 300 W Xe lamp with the distance of 10 cm at 25 °C. The light with the wavelength less than 420 nm was cut off. At the given intervals, the bacteria concentration was measured by direct plate counting. 100 uL bacteria solution was aspirated and diluted at gradient dilution with sterilized PBS, and the final concertatrion was 10^4 CFU/mL. Then, 100 uL diluted mixture was spread on a nutrient agar medium, and the colonies were counted to determine the viable bacterial numbers after being incubated at 37 °C for 18 ∼ 24 h. All of the survival experiments were repeated three times. In addition, the K^+ ion concentrations in bacteria solution after being centrifuged at 16000 rpm for 10 min were determined by ICP investigation. Total organic carbon (TOC) in the bacteria solution was measured at each interval on a Vario TOC analyzer. The active species during the photocatalytic reaction were investigated by additionally dissolving 0.050 mmol trapping agents including sodium oxalate, $KBrO_3$, *tert*-butanol and *p*-benzoquinone, which could capture photo-generated holes, photo-generated electrons, ·OH radical and ·O_2^- radical, respectively. The concentration of each scavenger was optimized to ensure the scavenging effect.

2.6. Microscopic observations of bacteria

(1) SEM analysis. The bacteria were firstly fixed on a silicon pellet with 2.5% glutaraldehyde solution at 4 °C for 4 h. After being washed for 15 min with 0.1 mol/L phosphoric acid for three times, the bacteria were fixed with 1% osmium tetraoxide for 6 h. The samples were sequentially dehydrated with 30%, 50%, 70%, 90%, and 100% ethanol for 15 min, respectively. Then, the CO_2 critical-point dried specimens were sputter-coated with gold and observed on FEHITACHI S-4800. (2) TEM analysis. After the fixture and dehydration process for SEM analysis, the specimens were embedded at 37 °C (12 h) and further fixed at 37 °C (12 h), 45 °C (12 h) and 60 °C (24 h), respectively. Then, the specimens were cut into slices of 50–60 nm, dyed with 3% uranyl acetate-lead citrate mixture and observed on JEM-2010. (3) The investigation of bacteria shape and size were also performed on a Veeco Multimode IIIa atomic force microscope (AFM) after the fixture and dehydration process for SEM observation. (4) Confocal laser fluorescence images were adopted to evaluate the bacteria survival. The bacteria cells were costained with LIVE/DEAD™ BacLight™ Bacterial Viability Kit (ThermoFisher Scientific, Shanghai, China). Calcene-AM was a typical green fluorescent stain that labeled live bacteria and PI was a red-fluorescent stain that labeled dead bacteria. After being kept in dark for 1 h, the bacteria were cleaned by PBS solution for twice and then imaged using a laser scanning confocal microscope (Leica TCS SP5-II). Calcein-AM and PI were excited by the lasers with the wavelength of 488 nm and 533 nm, respectively.

3. Results and discussion

3.1. Characterization of X%Ag/TiO₂-N catalysts

TG/DTA curves of 4.0%Ag/TiO₂-N in Fig. S1 presented little significant thermal signal and weight loss, suggesting the complete removal of organic residues and the excellent thermal stability of Ag/TiO₂-N composite against decomposition and phase change. It was in accordance with the FTIR spectra (Fig. S2), which revealed the similar absorbance bands in 4.0%Ag/TiO₂-N, 4.0%Ag/TiO₂ and TiO₂-N as that in pure TiO₂, around 3410, 1630 cm^{-1} (O−H bending vibration) [32] and 580 cm^{-1} (O-Ti stretching vibration) [33], respectively. It was resulted from the unique advantage of the supercritical solvothermal process to achieve the pure and stable catalysts without subsequent high-temperature thermal treatments. XRD patterns in Fig. 1 showed that the diffraction peaks in all samples could be assigned to the anatase TiO₂ phase (JCPDS21-1272). The characteristic peak of metallic Ag nanoparticles could not be found in all the Ag-contained samples, implying its small size and high dispersion on the surface of TiO₂. The XPS spectra in Fig. S3 could demonstrate that the metallic state of Ag species according to the binding energy around 367.7 and 373.7 eV in Ag $3d_{5/2}$ and Ag $3d_{3/2}$ with the difference of 6.0 eV [34,35]. Meanwhile, Raman spectra (Fig. S4) could confirm the incorporation of N-dopant with the TiO₂ lattice. Raman modes of E_g, E_g, B_{1g}, A_{1g} and E_g corresponding to anatase TiO₂ was around 144, 196, 396, 516, and 639 cm^{-1},
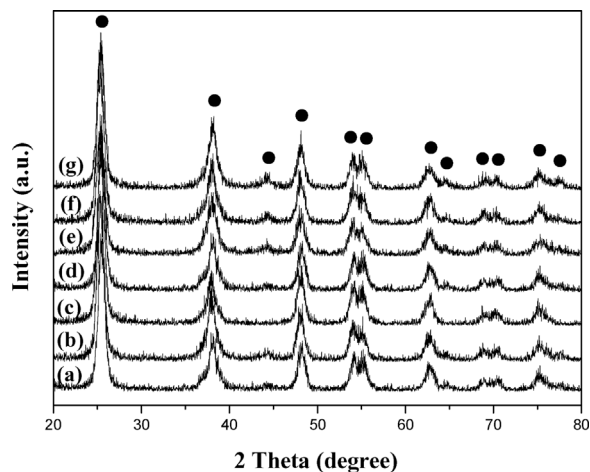

Fig. 1. XRD patterns of (a) TiO₂, (b) 4.0%Ag/TiO₂, (c) TiO₂-N, (d) 2.4%Ag/TiO₂-N, (e) 3.1%Ag/TiO₂-N, (f) 4.0%Ag/TiO₂-N and (g) 4.7%Ag/TiO₂-N samples.
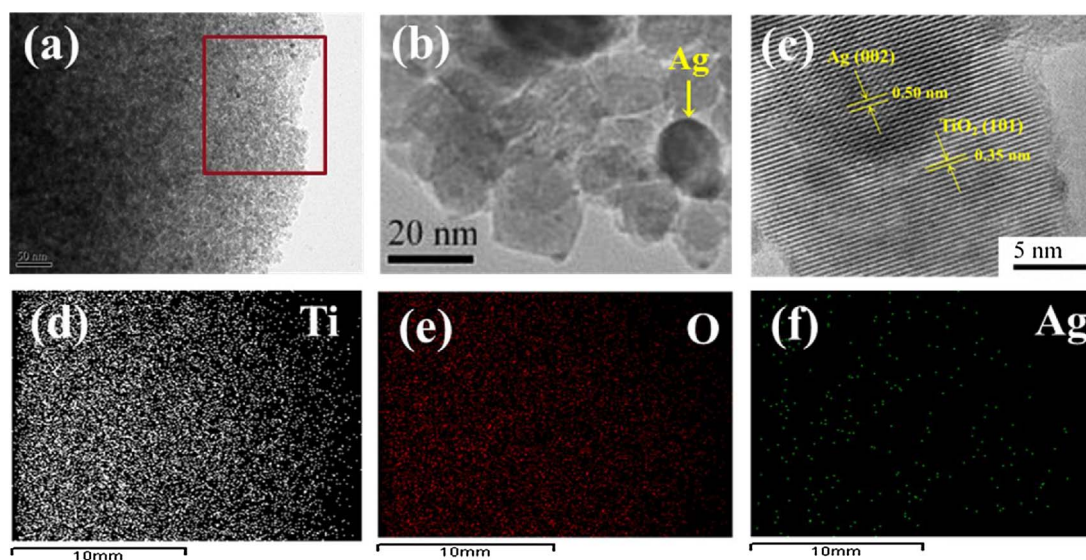
Fig. 2. (a, b) TEM and (c) HRTEM images of 4.0%Ag/TiO$_2$-N with chemical mapping of (d) Ti, (e) O, and (f) Ag elements.

respectively. The obvious shift of principal peak to the higher wave-number in N-doped samples indicated the increase of oxygen vacancies [36,37], mainly due to the partial replacement of O atoms with N atoms.

From the SEM image in Fig. S5, one could find that the morphology of 4.0%Ag/TiO$_2$-N sample presented in the shape of microspheres with the diameter of about 2.0 um. TEM images in Fig. 2 revealed that it was assembled by a huge number of well-distributed nanoparticles, which were constituted by the TiO$_2$-N substrate with the diameter of about 20 nm and the Ag nanoparticles with the diameter of about 15 nm. Although no reflection of the Ag phase could be observed in XRD patterns, HRTEM image in Fig. 2(c) demonstrated the high crystallization of metallic Ag phase (JCPDS41-1402) with the crystal lattice of 0.50 nm indicative of the (002) facet. The crystal lattice of 0.35 nm is corresponding to the (101) facet of anatase TiO$_2$. The distinct juncture between two crystal phases further confirmed the strong interaction between Ag nanoparticle and TiO$_2$-N. The chemical mapping images showed the uniform location of Ag nanoparticles on the surface of TiO$_2$-N catalyst.

Other structural parameters were summarized in Table 1. All the samples prepared *via* supercritical solvothermal process presented much higher S_{BET} than P25 TiO$_2$. It was ascribed that the porous structure in the precursors could be preserved in the supercritical fluid due to the absence of surface tension. TiO$_2$-N exhibited similar S_{BET}, V_P and D_P values to TiO$_2$ due to the low content of N-dopant. With the increase of Ag concentration in the samples, S_{BET} value of X%Ag/TiO$_2$-N samples gradually decreased with the slightly reduced V_P and D_P values. Thus, one could conclude that the Ag nanoparticles were mainly

located on the TiO$_2$-N surface rather than being deposited in the pore channels. It also illustrated the lower S_{BET} of 4.0%Ag/TiO$_2$ than that of pure TiO$_2$.

3.2. Optical performances

UV–vis DRS spectra (Fig. 3) showed that the pure TiO$_2$ displayed no significant absorbance in the visible-light region owing to its large band gap (3.2 eV). In comparison to the slight absorbance for visible light due to the N-doping in TiO$_2$, the loading of Ag nanoparticles could generate great enhancement of visible-light absorption *via* its surface plasma resonance [38,39]. In addition, 4.0%Ag/TiO$_2$-N presented the weakest PL intensity in comparison to other catalysts (Fig. S6), indicating the reduced recombination of the photo-induced electrons and holes by the electron trapping effect of Ag nanoparticles [40,41].

3.3. Antibacterial activity

The antibacterial activities of different photocatalysts were mainly investigated on *A. baumannii*, ATCC 19606. As shown in Fig. 4, neither visible light nor pure TiO$_2$ could present the antibacterial activity. As we known, the Ag nanoparticles could play the role of disinfection. As a result, X%Ag/TiO$_2$-N catalysts presented the gradually increased activity with the elevated Ag content in dark and the TiO$_2$-N or TiO$_2$
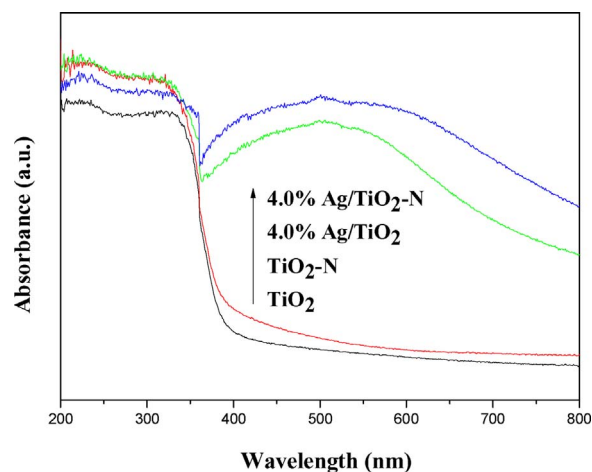
Table 1
Structure parameters of different samples.

Samples	S_{BET} (m^2/g)	V_p (cm^3/g)	D_p (nm)
P25 TiO$_2$	45	0.20	20
TiO$_2$	169	0.25	5.8
TiO$_2$-N	165	0.24	5.6
2.4%Ag/TiO$_2$-N	152	0.19	5.3
3.1%Ag/TiO$_2$-N	140	0.19	5.4
4.0%Ag/TiO$_2$-N	130	0.20	5.3
4.7%Ag/TiO$_2$-N	121	0.20	5.3
4.0%Ag/TiO$_2$	156	0.23	6.2
4.0%Ag/TiO$_2$-N(P)	56	0.10	5.3
4.0%Ag/TiO$_2$-N(I)	121	0.16	4.4
4.0%Ag/TiO$_2$-N(S)	101	0.10	4.0

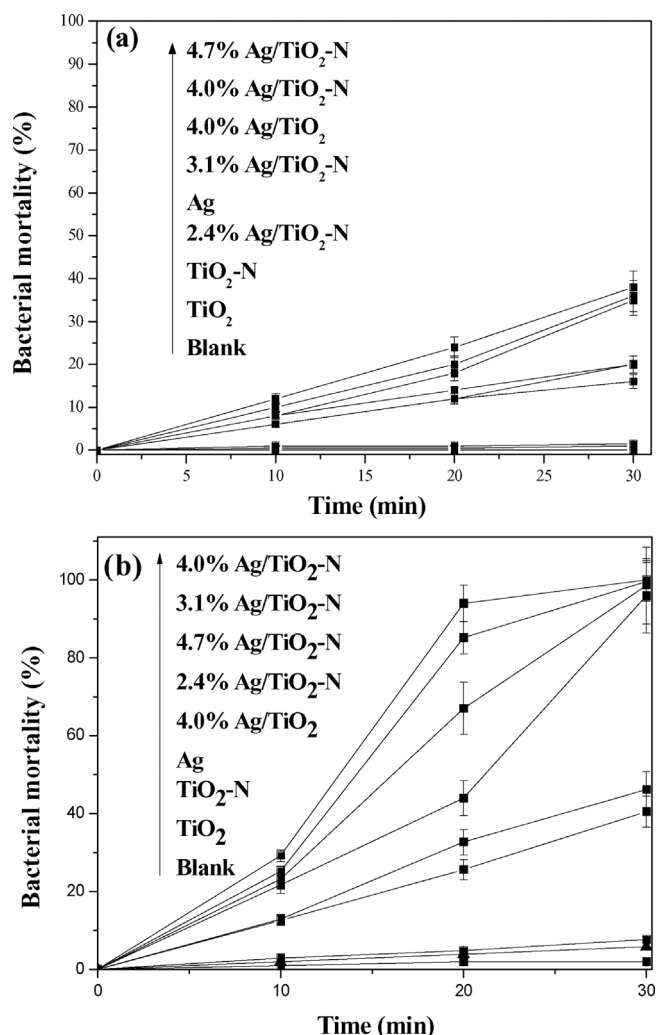**Fig. 3.** UV–vis DRS spectra of different samples.

Fig. 4. Antibacterial activities of different samples (a) in dark and (b) under visible-light irradiations (420 nm < λ < 780 nm). Reaction conditions: 0.090 mg catalyst, 15.0 mL 10^8 cfu/mL (0.5 MFC) A. *baumannii* (ATCC 19606), $T = 25$ °C, one 300 W Xe lamp.

implying the dispersion effect of TiO_2 substrate. In addition, no synergistic effect between Pt nanoparticles and TiO_2-N could be found (Fig. S7), since 4.0%Pt/TiO_2-N catalyst remained the low visible-light antibacterial activity as that in dark, clearing the prominent synergistic effect between Ag nanoparticles and TiO_2-N. From Fig. S8, we could find that other photocatalysts prepared by the different routes, including 4.0%Ag/TiO_2-N(P), 4.0%Ag/TiO_2-N(S) and 4.0%Ag/TiO_2-N(I) with the same Ag-content and similar TiO_2 crystallization as that of 4.0%Ag/TiO_2-N, showed the weaker visible-light antibacterial activity than 4.0%Ag/TiO_2-N. It further demonstrated the unique advantage of the supercritical solvothermal process for achieving the larger specific surface area (see Table 1) and the strong combination of Ag nanoparticles with TiO_2-N.

As we known, K^+ ion plays a vital role in the cell physiological activities [42], and thus the leakage of K^+ ion from the cell was monitored during the inactivation process to examine the change in cell membrane permeability [43]. Additionally, the TOC analysis was performed to investigate the actual mineralization of cell molecule. In Fig. S9, the concentration of leaked K^+ ions from bacteria cell increased significantly on 4.0%Ag/TiO_2-N catalyst with the prolonged irradiation time, and the TOC value simultaneously decreased sharply with the 76% removal. In comparison, little changes of both concentration of leaked K^+ ions and TOC value on Ag nanoparticles and TiO_2-N. Obviously, the synergistic effect of Ag and TiO_2-N in 4.0%Ag/TiO_2-N catalyst could not only result in the bacteria inactivation but also induce the complete decomposition of bacteria cell into inorganic compounds with the disrupted permeability of cell membrane. Consequently, the Na^+-k^+ pump was inactivated and the cellular metabolism was collapsed to generate enough adenosine triphosphate (ATP) [44,45].

In order to further understand the effect of each component in the catalyst, the antibacterial activities were investigated under light irradiations with different wavelengths. From Fig. S10, it could be found the higher UV-light photoactivity of 4.0%Ag/TiO_2-N, TiO_2-N, TiO_2, 4.0%Ag/TiO_2 and Ag nanoparticles than that of UV light, since TiO_2 was very active in UV-light region. Little obvious significance of Ag deposition and N-doping could be found for enhancing the activity. At the same time, the pure Ag nanoparticles combined with UV light achieved the improved activity, obviously due to their intrinsic antibacterial capability. Under the light irradiation at l = 500 nm, the antibacterial activity (see Fig. S11) was mainly induced by the disinfection effect of Ag nanoparticles *via* the effect of surface plasma resonance since all the Ag-contained samples showed the similar activity. Unexpectedly, 4.0%Ag/TiO_2-N presented the much higher near-infrared-light antibacterial activity than 4.0%Ag/SiO_2, Ag nanoparticles and TiO_2-N (Fig. S12), although TiO_2-N could not absorb the near-infrared light. It was probably ascribed that Ag nanoparticles absorb the near-infrared light (780–1100 nm) and generate hot electrons [46] to improve the photothermal effect [47] which could be further enhanced by the TiO_2-N substrate. In Fig. S13, the photothermal property measured on thermal infrared image demonstrated the enhanced near-infrared photothermal conversion property of 4.0%Ag/TiO_2-N with the increased surface temperature of 17 °C after irradiation for 185 s. It possibly attributed that TiO_2-N substrate could maintain the photothermal energy resulted from Ag nanoparticles to disinfect the bacteria, since Ag nanoparticles only presented the slightly increased temperature even in the case of 5 times amount and TiO_2-N revealed no photothermal effect. Fig. 5 compared the activity of both 4.0%Ag/TiO_2-N and Ag nanoparticles under light irradiations with different wavelength. Ag nanoparticles presented the much lower activity with the increase of light wavelength than in UV light region, mainly owing to its intrinsic antibacterial effect by disrupting the membrane respiratory electron transport chains and DNA replication components [48]. In comparison, 4.0%Ag/TiO_2-N showed the significantly improved activity under different light irradiation *via* the synergistic effect between Ag nanoparticles and TiO_2-N substrate. Especially, the activity of

catalyst only acted as the substrate like SiO_2 (see Fig. S7). In comparison, the N-dopant presented no influence to the activity in dark, according to the similar activity of 4.0%Ag/TiO_2-N to that of 4.0%Ag/TiO_2. More importantly, the activities of X%Ag/TiO_2-N catalysts were greatly enhanced under visible-light irradiations and 4.0%Ag/TiO_2-N showed the highest activity among all the catalysts. It was obviously owing to the synergistic effect between Ag nanoparticles and TiO_2-N, resulting from the stable combination of Ag nanoparticles and TiO_2-N *via* the supercritical solvothermal process. Besides, the high specific surface area, the enhanced visible-light absorption *via* the Ag surface plasma resonance, and the reduced recombination of the photo-induced electrons and holes *via* the electron trapping effect of Ag nanoparticles could efficiently improve the activity. Meanwhile, the gradually increased content of Ag led to the elevated activity, obvious due to the improved separation efficiency of photo-induced charges. However, the excessive loading of Ag nanoparticles in 4.7%Ag/TiO_2-N sample was harmful to the activity since the surface plasma resonance could be possibly diminished and the charge separation could be inhibited [40]. The significant higher activity of 4.0%Ag/TiO_2-N in comparison to that of 4.0%Ag/TiO_2 was owing to the stable combination of Ag nanoparticles with the TiO_2-N substrate *via* the silver-ammonia complexation process and the improved visible-light adsorption. Although the amount of Ag nanoparticles in 4.0%Ag/TiO_2 was very low, its visible-light photoactivity was similar to that of pure Ag nanoparticles, further
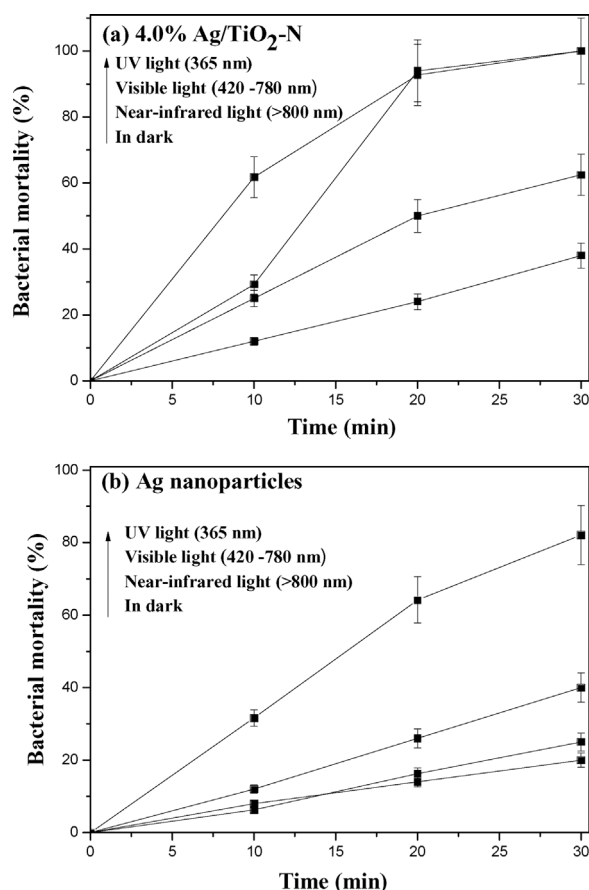
Fig. 5. Antibacterial activities of (a) 4.0%Ag/TiO$_2$-N and (b) Ag nanoparticles under different light irradiations or in dark. Reaction conditions were given in Fig. 4.

4.0%Ag/TiO$_2$-N in the visible-light region was high up to that in UV light region.

3.4. Study on the antibacterial process

In order to investigate the antibacterial process *via* visible-light photocatalysis, the active radicals during the photoreaction were investigated by the trapping test with different scavengers for h$^+$, ·OH, ·O$_2^-$ and e$^-$, respectively. All the scavengers could not generate inactivation activities to the bacterial cell under visible-light irradiations, as shown in Fig. S14. From Fig. 6, ·O$_2^-$ radical could be determined as the main active radical since photocatalytic antibacterial activity was greatly restrained after adding *p*-benzoquinone scavenger. It implied that Ag nanoparticles located on TiO$_2$-N substrate could promote more electrons to react with O$_2$ or H$_2$O and further benefit the formation of active ·O$_2^-$ radical. In addition, little leakage of Ag nanoparticles and dissolved Ag+ ions in 4.0%Ag/TiO$_2$-N could be found according to the ICP results, suggesting the synergistic effect of Ag nanoparticles and TiO$_2$-N was the dominant for the bacterial inactivation rather than the released Ag$^+$ ion.

The bacterial cell membrane contains essential protein components such as the permease system and respiratory chain, which can transport substrates and generate energy with functionalized electron chains, playing a vital role in bacterial metabolism [43]. Therefore, the morphology changes of A. *baumannii* bacteria during the photocatalytic antibacterial process were investigated in detail. According to SEM images in Fig. 7, the original A. *baumannii* displayed the shape of a plump rod with intact bacteria envelope before photocatalytic disinfection. With the increase of visible-light irradiation time, the surface of bacteria cell started to wrinkle and gradually became roughly sunken in
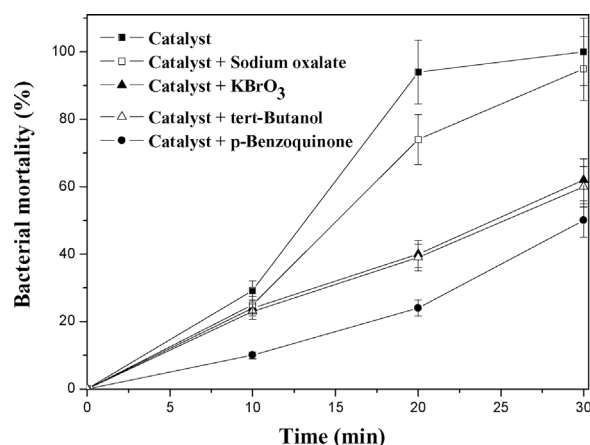

Fig. 6. Antibacterial activities of 4.0%Ag/TiO$_2$-N with and without scavengers under visible light irradiations (420 nm < λ < 780 nm). Reaction conditions were given in Fig. 4.
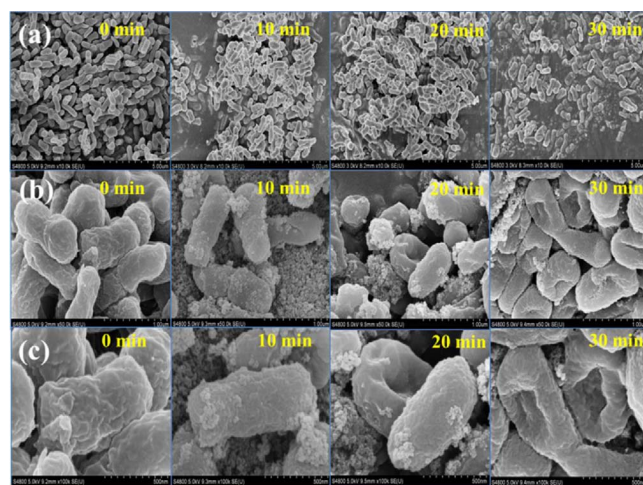

Fig. 7. SEM images of A. *baumannii* at different magnifications of (a) 10 K, (b) 50 K and (c) 100 K during the visible-light photocatalytic inactivation process on 4.0%Ag/TiO$_2$-N. Reaction conditions were given in Fig. 4.

the center. Finally, almost the entire cell surface was occupied by hollows and holes, indicative of the extreme destruction of the cell membrane of bacteria. As a result, the inner cell tissue of bacteria could be destroyed and the osmotic pressure was decreased [44]. It implied that the photocatalytic treatment could induce the size change of bacteria besides of the structural damage. It could be attributed that the inactivation patterns of membrane-bounded proteins during photocatalysis process, which was mainly due to the ·O$_2^-$ oxidation, may lead to conformational changes in membrane architecture and membrane dysfunction, and finally result in the cell death. TEM images in Fig. 8 showed the inner cell tissue, which was composed by the enzymatic structure to regulate the bacteria growth, was also gradually damaged during the photocatalytic process on 4.0%Ag/TiO$_2$-N catalyst, in comparison to the original bacteria with an intact cell envelope. The cell destruction process started from cell wall to intracellular components and the final collapse of the whole cells. The cell wall was decomposed and the rendered interior of the cell became white, indicating that the outer cell membrane was damaged leading to the leakage of the interior component with the central portion (cytoplasm) and causing the cell death. AFM images in Fig. S15 presented the topography changes of A. *baumannii*. The cell length of radial direction was decreased from 1016 to 586 nm and the thickness was simultaneously reduced sharply from 148 to 6.62 nm after photocatalytic treatment for 30 min on 4.0%Ag/TiO$_2$-N catalyst. Meanwhile, the obvious bacterial
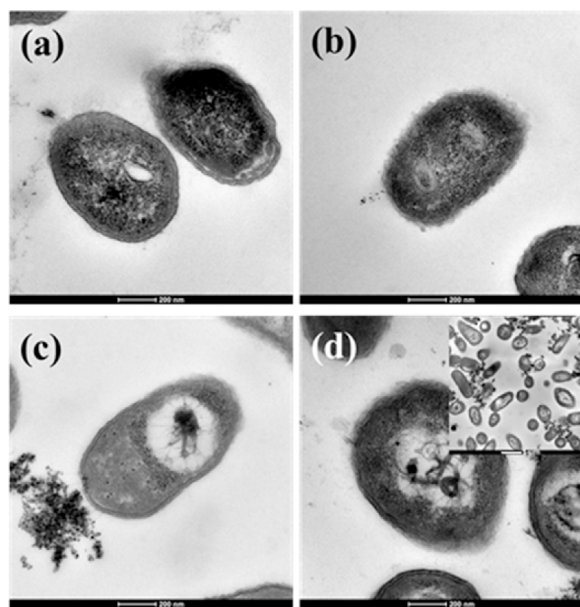
Fig. 8. TEM images of A. *baumannii* (a) before, and after photocatalytic disinfection for (b) 10 min, (c) 20 min and (d) 30 min on 4.0%Ag/TiO$_2$-N catalyst. The inserted image was obtained at the low magnification. Reaction conditions were given in Fig. 4.
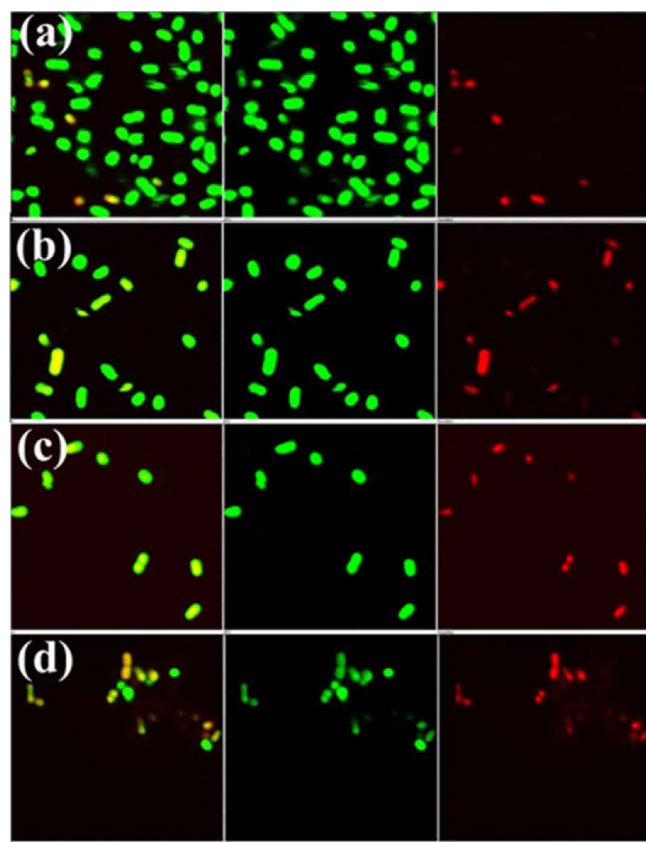

Fig. 9. Confocal fluorescent images recorded using dual color channels for live and dead of A. *baumannii* (a) before, and after photocatalytic treatment for (b) 10 min, (c) 20 min and (d) 30 min on 4.0%Ag/TiO$_2$-N catalyst. The live and dead cells are stained with SYTO9 (green) and PI (red) dye compounds, respectively. Reaction conditions were given in Fig. 4. (For interpretation of the references to colour in this figure legend, the reader is referred to the web version of this article.)

membrane destruction and intracellular content leakage could also be observed. To state the cellular survive-death mode during the 4.0%Ag/TiO$_2$-N photocatalytic inactivation, confocal fluorescent images were recorded in Fig. 9. Excluding the orange fluorescence emitted by 4.0%Ag/TiO$_2$-N catalyst, the live bacteria (green) were gradually replaced by the dead ones (red) with the increased treatment time. More importantly, the number of dead cells was simultaneously decreased with the reduced number of live ones, indicative of the mineralization effect of photocatalysis to the bacteria in addition to the inactivation effect, which was unlike other processes [49]. We could find all the above results of bacteria morphology changes were highly consistent with those obtained from the changes of TOC value and leaked K$^+$ content. As a result, photocatalytic disinfection could induce not only the conformational change of bacteria but also the fatal damage to the cell structure. Membrane proteins and cell inner contents were inactivated and mineralized through the photocatalytic process *via* the synergistic effect of Ag nanoparticles and TiO$_2$-N, leading to the membrane dysfunction and the final cell death.

We had known that the bacteria could immediately start a SOS response for self revovery after the emergency damages, such as loss of chromosomal DNA and membrane infiltration, which are lethal to the cells [50,51]. Therefore, the self-repair ability of the bacteria was measured *via* comparing the resurrection rate on different samples, as shown in Fig. S16. After an antibacterial experiment with further cultivation for 24 h, it was significantly found that no bacteria could be revived on 4.0%Ag/TiO$_2$-N catalyst, comparing to the 7% resurrection rate of bacteria on TiO$_2$-N and 20% on Ag nanoparticles. Obviously, 4.0%Ag/TiO$_2$-N was fatally destroyed the bacteria through fragmentized cells, and thus the cells lost their ability to synthesize ATP [51]. Both TiO$_2$-N and Ag nanoparticles were only able to induce the cell death rather than mineralizing the bacteria cell and blocking the synthesis of ATP.

In addition, 4.0%Ag/TiO$_2$-N catalyst simultaneously displayed much higher visible-light antibacterial activities than that in dark, against a variety of other clinical frequently encountered bacteria, such as Gram positive *Staphylococcus aureus* (*sau*, ATCC 29213 and 25923), Enterobacteriaceae bacteria *Escherichia coli* (*E. coli*, ATCC 25922 and 35218) and Nonfermentative bacteria *Pseudomonas aeruginosa* (*pac*, ATCC 27853), as shown in Fig. 10. It was indicative of the antibacterial universality *via* the synergistic effect of Ag nanoparticles and TiO$_2$-N, showing the potential for the large-scale application of disinfection.

4. Conclusions

This work developed the hybrid Ag/TiO$_2$-N photocatalyst prepared *via a* supercritical solvothermal process in ethanol fluid. During the synthesis process, the reduction of Ag$^+$ ions in silver-ammonia complex solution and N-doping were simultaneously achieved. As a result, the uniformly distributed Ag nanoparticles stably combined with the surface of TiO$_2$-N substrate and thus facilitated the visible light harvesting and the separation of photo-induced charges to improve the visible-light photocatalytic inactivation towards A. *baumannii*. The main active species was determined as $\cdot$O$_2^-$ radical according to the trapping test. The antibacterial activity in visible-light region could be mainly attributed to the synergistic effect of Ag nanoparticles and TiO$_2$-N substrate, in comparison to the inactivation activity of both Ag nanoparticles and TiO$_2$-N under UV light irradiation. The antibacterial activity in near-IR light region was greatly resulted from the photothermal effect of Ag nanoparticles, which could be remained by the TiO$_2$-N substrate. The synergistic Ag/TiO$_2$-N photocatalytic systems led to the complete destroy and mineralization of A. *baumannii* bacteria and eliminated its self-repair system. Additionally, the great inactivation
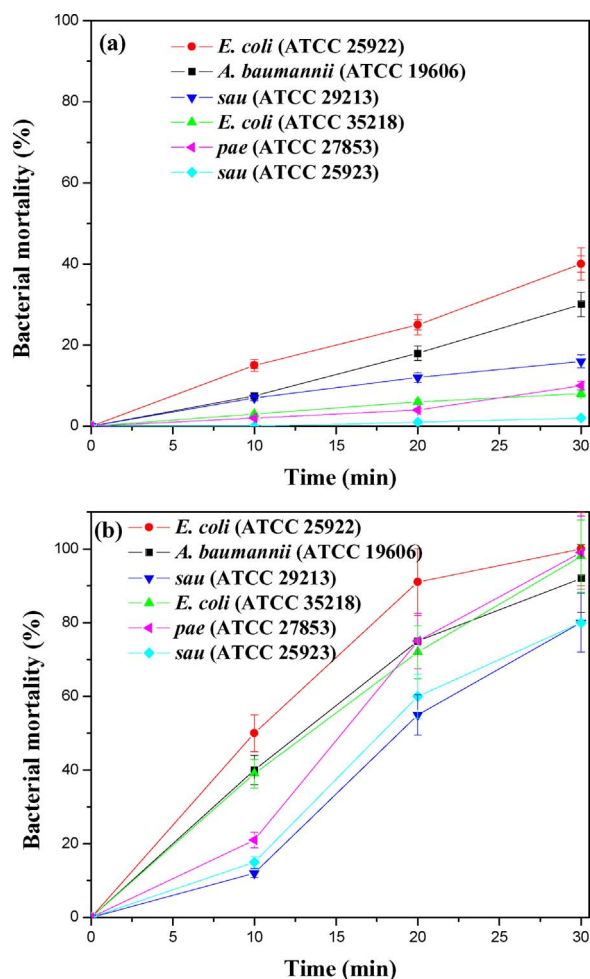
Fig. 10. Antibacterial performance for different bacteria on 4.0%Ag/TiO$_2$-N catalyst (a) in dark and (b) under visible-light irradiation (420 nm $<\lambda<$ 780 nm). Reaction conditions: 0.090 mg catalyst, 15.0 mL 10^8 cfu/mL (0.5 MFC) bacteria suspension, T = 25 °C, one 300 W Xe lamp.

ability of Ag/TiO$_2$-N photocatalyst for various bacteria implied the significant potential in the practical application in the medical environments.

Appendix A. Supplementary data

Supplementary data associated with this article can be found, in the online version, at http://dx.doi.org/10.1016/j.apcatb.2017.10.052.

References

[1] S.S. Philip, J.W. Costerton, E.P. Greenberg, Science 284 (1999) 1318.

[2] X.C. Meng, Z.S. Zhang, J. Catal. 344 (2016) 616.
[3] T.Z. Tong, A. Shereef, J.S. Wu, C.T.T. Binh, J.J. Kelly, J. Gaillard, K.A. Gray, Environ. Sci. Technol. 47 (2013) 12486.
[4] M.J. Lima, A.M.T. Silva, C.G. Silva, J.L. Faria, J. Catal. 353 (2017) 44.
[5] N.F. Adegboyega, V.K. Sharma, K.M. Siskova, R. Vecerova, M. Kolar, R. Zboril, J.L. Gardea-Torresdey, Environ. Sci. Technol. 48 (2014) 3228.
[6] C. Sichel, J. Blanco, S. Malato, P. Fernandez-Ibanez, J. Photochem. Photobiol. A 189 (2007) 239.
[7] M.R. Hoffmann, S.T. Martin, W. Choi, D.W. Bahnemann, Chem. Rev. 95 (1995) 69.
[8] H. Choi, D. Shin, B.C. Yeo, T. Song, S.S. Han, N. Park, S. Kim, ACS Catal. 6 (2016) 2745.
[9] V. Vaiano, O. Sacco, D. Sannino, P. Ciambelli, Appl. Catal. B 170 (2015) 153–161.
[10] M.H. Li, M.E. Noriega-Trevino, N. Nino-Martinez, C. Marambio-Jones, J.W. Wang, R. Damoiseaux, F. Ruiz, E.M.V. Hoek, Environ. Sci. Technol. 45 (2011) 8989.
[11] D. Gumy, C. Morais, P. Bowen, C. Pulgarin, S. Giraldo, R. Hajdu, J. Kiwi, Appl. Catal. B 63 (2006) 76.
[12] M. Cho, H. Chung, W. Choi, J. Yoon, Water Res. 38 (2004) 1069.
[13] J.R. Morones, J.L. Elechiguerra, A. Camacho, K. Holt, J.B. Kouri, J.T. Ramirez, M.J. Yacaman, Nanotechnology 16 (2005) 2346.
[14] K. Page, R.G. Palgrave, I.P. Parkin, M. Wilson, S.L.P. Savin, A.V. Chadwick, J. Mater. Chem. 17 (2007) 95.
[15] X.G. Hou, H.Y. Ma, F. Liu, J.H. Deng, Y.K. Ai, X.L. Zhao, D. Mao, D.J. Li, B. Liao, J. Hazard. Mater. 299 (2015) 59.
[16] Y. Jiang, D. Liu, M.J. Cho, S.S. Lee, F.Z. Zhang, P. Biswas, J.D. Fortner, Environ. Sci. Technol. 50 (2016) 2514.
[17] D.H. Kuo, W.T. Hsu, Y.Y. Yang, Appl. Catal. B 184 (2016) 191–200.
[18] K. Fujiwara, Y. Deligiannakis, C.G. Skoutelis, S.E. Pratsinis, Appl. Catal. B 154-155 (2014) 9.
[19] M.K. Devaraju, I. Honma, Adv. Energy Mater. 2 (2012) 284.
[20] R.H. Sui, P. Charpentier, Chem. Rev. 112 (2012) 3057.
[21] J.A. Darr, M. Poliakoff, Chem. Rev. 99 (1999) 495.
[22] J.T. Han, Y.H. Huang, X.J. Wu, C.L. Wu, W. Wei, B. Peng, W. Huang, J.B. Goodenough, Adv. Mater. 18 (2006) 2145.
[23] A. Sahraneshin, S. Takami, D. Hojo, K. Minami, T. Arita, T. Adschiri, J. Supercrit. Fluids 62 (2012) 190.
[24] T. Adschiri, Y. Hakuta, K. Arai, Ind. Eng. Chem. Res. 39 (2000) 4901.
[25] D.M. Kempaiah, D. Rangappa, I. Honma, Chem. Commun. 48 (2012) 2698.
[26] G. Aksomaityte, F. Cheng, A.L. Hector, J.R. Hyde, W. Levason, G. Reid, D.C. Smith, J.W. Wilson, W.J. Zhang, Chem. Mater 22 (2010) 4246.
[27] J.A. Gaddy, A.P. Tomaras, L.A. Actis, Infect. Immun. 77 (2009) 3150.
[28] A.Y. Peleg, H. Seifert, D.L. Paterson, Clin. Microbiol. Rev. 21 (2008) 538.
[29] L. Dijkshoorn, A. Nemec, H. Seifert, Nat. Rev. Microbiol. 5 (2007) 939.
[30] F. Perez, A.M. Hujer, K.M. Hujer, B.K. Decker, P.N. Rather, R.A. Bonomo, Antimicrob. Agents Chemother. 51 (2007) 3471.
[31] J.S. Lee, J.C. Lee, C.M. Lee, I.D. Jung, Y.I. Jeong, E.Y. Seong, H.Y. Chung, Y.M. Park, Biochem. Pharmacol. 74 (2007) 86.
[32] Y. Kuroda, T. Mori, K. Yagi, N. Makihata, Y. Kawahara, M. Nagao, S. Kittaka, Langmuir 21 (2005) 8026.
[33] Y. Tanaka, M. Suganuma, J. Sol-Gel Sci. Technol. 22 (2001) 83.
[34] H. Cheng, B. Huang, P. Wang, Z. Wang, Z. Lou, J. Wang, X. Qin, X. Zhang, Y. Dai, Chem. Commun. 47 (2011) 7054.
[35] M. Banerjee, P. Sachdev, G.S. Mukherjee, J. Appl. Phys. 111 (2012) 094302.
[36] K.R. Zhu, M.S. Zhang, Q. Chen, Z. Yin, Phys. Lett. A 340 (2005) 220.
[37] H.M. Liu, W.S. Yang, Y. Ma, Y.A. Cao, J.N. Yao, J. Zhang, T.D. Hu, Langmuir 19 (2003) 3001.
[38] A.B. Jasso-Salcedo, G. Palestino, V.A. Escobar-Barrios, J. Catal. 318 (2014) 170.
[39] D.B. Ingram, S. Linic, J. Am. Chem. Soc. 133 (2011) 5202.
[40] F. Gonell, M. Haro, R.S. Sanchez, P. Negro, I. Mora-Sero, J. Bisquert, B. Julian-Lopez, S. Gimenez, J. Phys. Chem. C 118 (2014) 11279.
[41] A.K. Jena, P. Bhargava, Renew. Energy 53 (2013) 265.
[42] T. Saito, T. Iwase, J. Horie, T. Morioka, J. Photochem. Photobiol. 14 (1992) 369.
[43] H.W. Sun, G.Y. Li, X. Nie, H.X. Shi, P.K. Wong, H.J. Zhao, T.C. An, Environ. Sci. Technol. 48 (2014) 9412.
[44] J. Li, J. Xu, W.L. Dai, K. Fan, J. Phys, Chem. C 113 (2009) 8343.
[45] H. Zhang, G. Wang, D. Chen, X. Lv, J. Li, Chem. Mater. 20 (2008) 6543.
[46] D. Liu, D. Yang, Y. Gao, J. Ma, R. Long, C.M. Wang, Y.J. Xiong, Angew. Chem. Int. Ed. 55 (2016) 4577.
[47] P. Christopher, H.L. Xin, S. Linic, Nature Chem. 3 (2011) 467.
[48] S. Silver, FEMS Microbiol. Rev. 27 (2003) 341.
[49] W.J. Wang, X.Q. Chen, G. Liu, Z.R. Shen, D.H. Xia, P.K. Wong, Appl. Catal. B 176 (2015) 444.
[50] Y.M. Chen, A.H. Lu, Y. Li, L.S. Zhang, H.Y. Yip, H.J. Zhao, T.C. An, P.K. Wong, Environ. Sci. Technol. 45 (2011) 5689.
[51] F. Bosshard, M. Bucheli, Y. Meur, T. Egli, Microbiology 156 (2010) 2006.